Applied Surface Science 711 (2025) 164089

Contents lists available at ScienceDirect

Applied Surface Science

journal homepage: www.elsevier.com/locate/apsusc

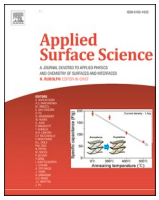

Full Length Article

The influence of oxyethylene groups on the performance of alkyl ether carboxylates at the CO_2/water interface

Jun Zhou [a,*], Shaopeng Li [b], Pengfei Wang [c], Ke Gao [a,*]

[a] Department of Earth and Space Sciences, Southern University of Science and Technology, Shenzhen 518055 Guangdong, China
[b] National Key Laboratory of Deep Oil & Gas (China University of Petroleum (East China)), Qingdao 266580 Shandong, China
[c] Advanced Institute for Ocean Research, Institute of Major Scientific Facilities for New Materials, Southern University of Science and Technology, Shenzhen 518055, China

ARTICLE INFO

Keywords:
Foam stability
CO_2/water interface
Carboxylate surfactants
Ethoxylated chain length
Molecular dynamics simulation
Interfacial behaviors

ABSTRACT

Understanding the interfacial behavior of surfactants at the CO_2/water interface is essential for optimizing foam-based technologies in carbon sequestration and enhanced oil recovery. This study employs molecular dynamics simulations to investigate how the ethoxylated chain length of carboxylate surfactants (AECs) govern interfacial dynamics and molecular transport characteristics. Results reveal that increasing ethylene oxide (EO) units enhances surfactant hydration, interfacial adsorption energy, and hydrogen bonding with water, promoting the formation of dense and elastic monolayers. These structural changes significantly reduce interfacial tension and retard lateral diffusion, thereby improving foam stability. However, elevated temperature conditions weaken the hydrogen-bond network and accelerate surfactant desorption, potentially compromising foam integrity. Furthermore, long EO chains create hydrated barriers that restrict CO_2 and water molecule diffusion across the interface, while short EO chains facilitate rapid molecular exchange. The presence of divalent cations (e.g., Ca^{2+}) further modulates interfacial dynamics by anchoring carboxylate groups and reducing mobility. These findings offer molecular-level insights into how EO chain length serves as a tunable parameter for tailoring interfacial film structures, dynamics, and gas–liquid transport behavior. This work provides valuable guidance for the design of CO_2/water foams with enhanced performance under reservoir-relevant conditions.

1. Introduction

CO_2-enhanced oil recovery is widely recognized for its dual benefits of improving hydrocarbon production while enabling long-term geological carbon storage [1,2]. Nevertheless, in heterogeneous reservoirs, direct CO_2 injection suffers from poor mobility control due to its low density and viscosity, leading to gravity override, viscous fingering, and early gas breakthrough [3,4]. To overcome these issues, CO_2/water (C/W) foam injection has been proposed as an effective mobility control strategy, increasing gas-phase apparent viscosity and improving sweep efficiency [5–7]. Despite these advantages, the stability of C/W foams under high-temperature and high-salinity (HT/HS) conditions remains a critical barrier to field application [8–10].

As metastable two-phase systems, C/W foams spontaneously degrade via drainage, coarsening and coalescence [11]. Surfactant are thus essential to promote foam generation and extend foam lifetime by reducing interfacial tension and stabilizing lamellae through steric hindrance and Marangoni-driven redistribution [12,13]. However, under HT/HS conditions, conventional surfactants face limitations: anionic types such as alkyl sulfonates or carboxylates tend to precipitate in brines with multivalent ions, while nonionic types like polyethylene oxides (PEO) degrade thermally above 80 °C [13,14]. Extended surfactants with ethylene oxide (EO) spacers have emerged as promising alternatives, offering tunable hydration shells that enhance salt resistance and interfacial performance [15,16]. Notably, EO chain length plays a critical role: shorter chains facilitate dense interfacial packing and rapid adsorption, while longer chains improve hydration and ion shielding [17]. This length-dependent trade-off leads to non-monotonic foam stability, whose molecular mechanism remains unclear.

Existing studies primarily evaluate C/W foam stability and underlying mechanisms through macroscopic metrics such as half-life, coarsening rates, and interfacial/bulk rheology [18,19]. Nevertheless, these parameters lack spatial and temporal resolution to reveal interfacial surfactant monolayer dynamics, which is essential to understand

* Corresponding authors.
E-mail addresses: jzhou@sustech.edu.cn (J. Zhou), gaok@sustech.edu.cn (K. Gao).

https://doi.org/10.1016/j.apsusc.2025.164089
Received 8 May 2025; Received in revised form 13 July 2025; Accepted 16 July 2025
Available online 17 July 2025

the influence of surfactant structure on foam stability. Molecular dynamics (MD) simulations provide atomistic insights into surfactant organization, water structuring, and interfacial forces [20,21]. For example, Ziolek et al. demonstrated that increasing surfactant surface density promotes interfacial water structuring and reduces mobility, thereby improving film rigidity [22]. Kanduč et al. further revealed the presence of dynamic hydrogen-bond networks between interfacial surfactant molecules, known as the hydrogen belts, which could contribute to film cohesion through continuous bond rearrangement [23]. Our earlier work further demonstrated how multi-component mixtures, including surfactant-polymer and surfactant-nanocellulose composites, modulate interfacial water dynamics and supramolecular architecture [24,25]. These findings collectively establish that beyond interfacial tension reduction, foam stability is governed by supramolecular structuring and confined solvent behavior within foam films.

Among extended surfactants, alkyl ether carboxylates (AECs) show excellent foaming ability and salt tolerance, making them attractive for C/W foam applications [26]. Yet, the molecular-level effects of EO chain length on their interfacial adsorption, hydration, and structural dynamics remain poorly understood. In this work, we employ MD simulations to systematically investigate how EO chain length affects AEC surfactant organization and interfacial water dynamics at the C/W interface. By correlating surfactant structure with interfacial organization and water mobility, our work aims to provide molecular-level insights that inform rational design of high-performance surfactants for C/W foam stabilization in HT/HS reservoir conditions.

2. Materials and methods

2.1. Materials

AEC surfactant with varying EO chain lengths (3, 6, 9, 12, and 15) were generously provided by Yonghong Material (Shandong, China) and used without further purification. Foaming solutions were prepared using high-purity water purchased from Wahaha Group Co., Ltd. (Hangzhou, China) at room temperature (25 ± 2 °C) and then stored at 50 °C for at least 12 h prior to use.

2.2. C/W foam stability measurement

The Waring blender method was employed to evaluate the stability of C/W foam generated by previously mentioned AEC surfactants with a concentration of 0.5 wt%. Briefly, 25 mL of the foaming solution was placed in the blender cup and purged with CO_2 for 10 min to reach gas–liquid equilibrium at atmospheric pressure. Foam was then generated by blending at 10,000 rpm for 3 min. Immediately after foaming, the foam was transferred to a sealed graduated cylinder to minimize liquid evaporation and interfacial disruption. Foam volume and liquid drainage half-life were subsequently recorded under ambient conditions for further analysis.

2.3. C/W interfacial tension measurement

The C/W interfacial tension (IFT) was measured using a custom-built high-pressure pendant drop tensiometer equipped with a sapphire-windowed cell. The apparatus allows precisely control of temperature (up to 150 °C) and pressure (up to 20 MPa). In each measurement, CO_2 and surfactant solutions were loaded subsequently into the cell, and the system was equilibrated at 50 °C and 20 MPa. IFT values were extracted by the analyzing the axisymmetric drop profiles using the Young-Laplace equation via *OpenDrop*, an open-source software package [27]. For each condition, the measurement was repeated three times, and the average value along with the standard deviation was reported.

2.4. MD simulations section

2.4.1. Models and simulation settings

This study investigates six AECs with varying EO chain lengths (Fig. 1a). The wavefunction of each molecule was generated using Gaussian16 program at the B3LYP/6-311+G** level [28]. To incorporate aqueous solvation effects, the solvation model based on the polarized continuous quantum mechanical charge density (SMD) [29] was employed during optimization, which could capture the bulk dielectric response characteristic of liquid water, enabling precise characterization of electrostatic environments around hydrophilic headgroups. Subsequent analyses of utilized Multiwfn (Function 12) package [30–32] to quantify molecular surface properties.

To model the C/W interface at 20 MPa, a typical "sandwich" structure (Fig. 1b) was constructed using the Packmol package [33], with dimensions of $10 \times 10 \times 25$ nm^3 along the x, y, and z axes, respectively, and a central water slab thickness of 4.0 nm (see Section 1 in Supporting Information). To model a saturated C/W interface, 100 surfactant molecules (corresponding to approximately 1.0 nm^2 per molecule) were initially positioned at interface, with all carboxylate headgroups oriented toward the aqueous phase. The centered aqueous slab, composed of 19,658 water molecules, was flanked by 8,124 CO_2 molecules on each side to provide adequate bulk phase volume. Sodium counterions (Na^+), equaling the number of surfactant molecules, ensured charge neutrality. For high-salinity systems, additional salt ions (Na^+, Ca^{2+}, and Cl^-) were randomly distributed within the aqueous phase using standard insertion algorithms to achieve target ionic concentrations, with steric conflicts resolved during energy minimization. The CHARMM General Force Field (CGenFF) was applied to model surfactants and ions [34–36], while the TIP3P and EPM2 models [37] were used for water and CO_2 molecules, respectively.

In the MD simulations, each system was relaxed under the NP_zT ensemble for 50 ns, during which the interface (xy plane) was fixed, and a compressibility value of 4.5×10^{-5} bar^{-1} was applied along the z direction. The system was then equilibrated under the NVT ensembles for an additional 50 ns, with trajectory and energy data from the last 30 ns used for subsequent analysis. Pressure was maintained at 20 MPa using the stochastic cell rescaling barostat with a coupling time of 5.0 ps [38], and three temperature points (323.15 K, 353.15 K, 383.15 K) were studied using the V-rescale thermostat with a coupling time of 0.5 ps [39]. A cutoff radius of 1.4 nm was applied for non-bonded interactions, and long-range electrostatic interactions were calculated using the particle-mesh Ewald (PME) method [40]. All simulations were performed using the GROMACS package (version 2023.03) [41,42] with a timestep of 2.0 fs. Interfacial configurations were rendered using Visual Molecular Dynamics (VMD) software [43].

2.4.2. Interfacial thickness and surface tension

In C/W interfacial systems, the molecular distribution is inhomogeneous, particularly near the interface. In this study, interfacial CO_2 and water molecules were identified using the ITIM algorithm implemented in the Pytim package [44,45]. A probe sphere radius of 0.2 nm was selected, with a cluster cutoff of 0.35 nm to exclude molecules far from the interface. The interface position was determined by the peak of the density profile, while the thickness of the interfacial zone was calculated as the full width at half maximum (FWHM) of the Gaussian distribution of interfacial molecules.

Interfacial tension was determined from the principal components of the stress tensor using the relation:

$$\gamma = \frac{L_z}{2}\left(P_{zz} - \frac{P_{xx} + P_{yy}}{2}\right)$$

where the P_{xx}, P_{yy}, and P_{zz} are the normal stresses in the x, y, z directions, respectively, and L_z is simulation cell length in the z direction. The stress tensors were obtained using the *gmx energy* command. The final

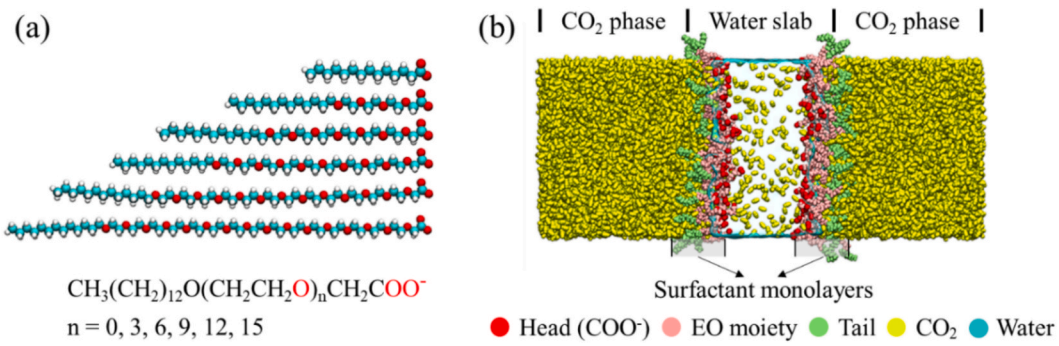

Fig. 1. (a) The molecular model of AEC surfactants, and (b) the configuration of the C/W interface with adsorbed AEC surfactants, Color code: red = the head group, pink = the EO moiety, lime = the tail group, cyan = the water slab, and yellow = the CO_2 molecule. Counterions and water molecules are omitted for clarity.

interfacial tension value represents time-averaged principal stresses, calculated for every 10 ns interval over the entire 30 ns NVT simulations, with error determined as the standard deviation of these values.

2.4.3. Detaching energy of surfactants

The detaching energy of a single surfactant was derived from the potential of mean force (PMF), obtained through a series of umbrella sampling simulations [46]. In these simulations, the surfactant was pulled away from the surface monolayer along the *z* direction using an umbrella potential, with a harmonic force constant of 1500 kJ/mol and a pull rate of 0.01 nm/ps. Umbrella sampling windows were generated by extracting frames from the pulling trajectory at 0.1 nm intervals of center-of-mass distance. Each sampling window was simulated for 1 ns, and the weighted histogram analysis method (WHAM) was used to compute the PMF along the reaction coordinate. Simulations were repeated three times, and the final detaching energy was reported as the average of these trials.

2.4.4. Dynamic behaviors of the confined interfacial molecules

To investigate the influence of the surfactant monolayer on the motion of confined interfacial molecules, the survival probability (SP) [47] and the mean square displacement (MSD) [48] were evaluated using the MDAnalysis Python package (MSD package in water dynamics analysis modules) [49,50]. Due to the confined effect of surfactants, the MSD of interfacial molecules is expected to be anisotropic, with distinct motion perpendicular and parallel to the *xy* plane. Here, we focus on the overall behavior, considering only repeated atoms (e.g. O atom in water, and C atom in CO_2) per frame, with an interval (dt) between frames. The self-diffusion coefficient for both interfacial and bulk molecules was then derived from the MSD calculations. For the motion of AEC monomers at the C/W interface, their MSD was directly obtained using the built-in *gmx msd* command.

Additionally, the hydrogen bond analysis module [51] in MDAnalysis package was employed to examine hydrogen bond networks near the interface. The default hydrogen bond criteria in GROMACS were applied: (i) the donor–acceptor distance is less than 0.35 nm, and (ii) the hydrogen-donor–acceptor angle is less than 30°. The dynamic behaviour of the hydrogen bonds was analyzed by calculating their average lifetime based on the time autocorrelation function [52]:

$$C(\tau) = \left\langle \frac{h_{ij}(t_0)h_{ij}(t_0+\tau)}{h_{ij}(t_0)^2} \right\rangle$$

where h_{ij} indicates the presence of a hydrogen bond between atom *i* and *j* (with $h_{ij} = 1$ if a hydrogen bond exists and $h_{ij} = 0$ otherwise). The function was evaluated over a maximum period (τ) from the starting time (t_0) in the trajectory. The hydrogen bond lifetime was obtained by fitting a biexponential function to the time autocorrelation curve:

$$C_c(\tau) \approx Ae^{-t/\tau_1} + (1-A)e^{-t/\tau_2}$$

where τ_1 and τ_2 represent time constants corresponding to short- and longer-timescale process, respectively. The code for these calculations is included in the MDAnalysis package.

3. Results and discussion

3.1. Foamability and foam stability of AECs

The interfacial performance of AEC surfactants at C/W interfaces is critically governed by the length of EO chain, which modulates hydrophilicity, solubility, and interfacial assembly dynamics. As shown in Fig. 2a, a marked solubility transition is observed upon incorporation of EO units into alkyl carboxylates. Although the addition of three EO groups (EO3) partially enhances hydrophilicity, it fails to sufficiently improve hydration capacity, leading to surfactant aggregation and floc formation. However, beyond this critical threshold (6–15 EO), the extended EO chains promote hydrogen bonding and dipole–dipole interactions with water molecules, resulting in clear solutions with homogeneous molecular dispersion.

This solubility trend directly affects foam generation and stability, as illustrated in Fig. 2b. The poor foamability of AEO_3C can be attributed to kinetic barriers caused by precipitation or bulky aggregate formation, which limit the diffusion of surfactant monomers to C/W interfaces. As the EO groups increase (6–9 EO), enhanced solubility facilitates rapid monomer adsorption at bubble surfaces, progressively improving foamability. The subsequent plateau beyond EO9 suggests a saturation effect in interfacial packing, where additional EO units no longer yield significant reductions in surface tension. A similar EO-dependent pattern is observed in drainage stability. The near plateau in drainage half-life at $\geq$ 9 EO groups implies the formation of cohesive interfacial films with enhanced mechanical strength, arising from two synergistic mechanisms: (1) steric stabilization via hydrated EO loops that protrude into the aqueous phase, impeding liquid drainage, and (2) intermolecular entanglement of EO chains, which increases interfacial viscoelasticity. Overall, the experimental findings demonstrate that AEC surfactants with 9 EO units achieve an optimal balance between interfacial adsorption kinetics and film stabilization, effectively integrating favorable solubility and diffusivity with enhanced steric and rheological properties at the interface. To further provide molecular-level insight into these performance trends, molecular dynamics (MD) simulations were conducted to systematically examine the interfacial organization, adsorption stability, and transport behavior of AEC surfactants with different EO chain lengths at the C/W interface.

3.2. Static properties at the C/W interface

3.2.1. Surface analysis of AECs

Alkyl carboxylates are classical amphiphilic molecules composed of a polar carboxylate head group ($-COO^-$) and a hydrophobic C13 alkyl tail.

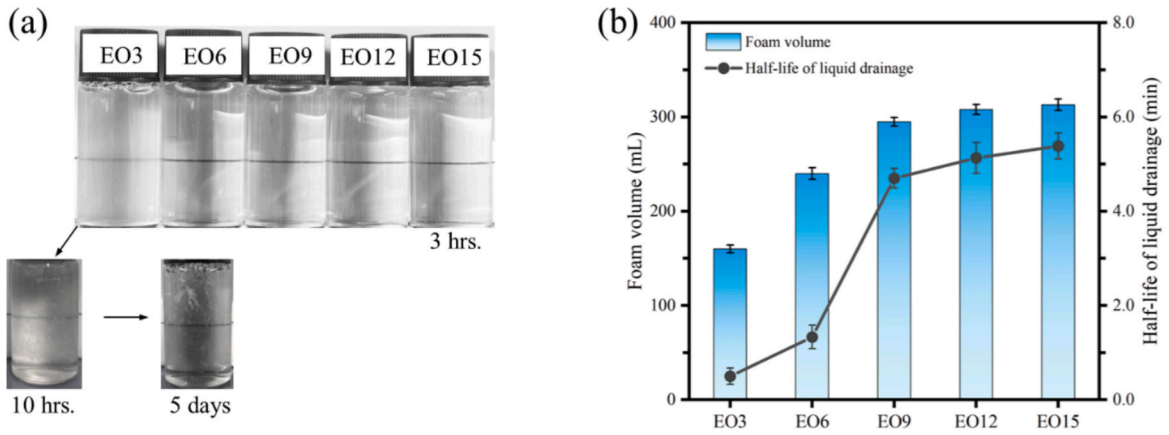

Fig. 2. (a) Solutions of AEC surfactants with varying EO groups, and (b) foamability and liquid drainage half-life of C/W foams stabilized by these AECs.

Incorporation of EO units (–OCH_2CH_2–) into the molecular backbone systematically alters their hydrophilic-lipophilic balance and interfacial assembly behavior. To elucidate the relationship between molecular structure and interfacial properties, electrostatic potential (ESP) surface analysis was conducted (see Section 2 in Supporting Information), and polarity variations were quantitatively evaluated using the molecular polarity index (MPI) [53], defined as:

$$\mathrm{MPI} = (1/A)\iint_S |V(\boldsymbol{r})|\,dS$$

where A and $V(\boldsymbol{r})$ refer to the area of vdW surface and value of ESP at a point $\mathbf{r}$ in space, respectively. The integration is performed over the whole molecular vdW surface (S).

As shown in Fig. 3 and Table S1, an inverse relationship is observed between MPI and molecular volume with increasing EO chain length. Quantitative analysis reveals that EO extension induces a 250.5 % increase in molecular volume (0.369 → 1.293 nm^3), accompanied by a 60.3 % reduction in MPI (53.94 → 21.38 kcal/mol), highlighting a trade-off between steric expansion and polarity attenuation. This antagonistic relationship can be attributed to two synergistic effects: (i) flexible EO chains adopt extended conformations that increase surface area and spatially distribute electrostatic charges, thereby reducing local polarity; and (ii) EO ether oxygens form hydrogen-bonded hydration shells that electrostatically screen the carboxylate group. Notably, the linear correlation between EO number and molecular volume ($R^2 > 0.98$) demonstrates the tunability of molecular architecture via EO incorporation. The resulting increase in steric bulk imposes geometric constraints during micellization, shifting the dominant stabilization mechanism from electrostatic interactions to entropy-driven assembly, offering critical insights for the rational design of surfactant-based colloidal systems.

3.2.2. Eo-dependent C/W interfacial tension

The IFT at the C/W interface, a critical parameter reflecting surfactant efficacy in foam stabilization, demonstrates a pronounced dependence on EO chain length under high-pressure and high-temperature (HPHT) conditions. While MD simulations are widely employed to complement experimental measurements of IFT, it is important to recognize that the computed values are highly sensitive to the assumed surface coverage of surfactant molecules. In this study, simulations were performed at a fixed surface excess of 1.0 nm^2 per molecule, which may not fully reflect the actual adsorption behavior under experimental conditions at a fixed concentration of 0.5 wt% (well above the critical micelle concentration). Previous studies suggest that the minimum adsorption area for these AEC surfactants under similar conditions is approximately 0.8 nm^2 per molecule [54], although this value is expected to vary with EO chain length due to changes in molecular conformation and interfacial packing efficiency (see Section 3 in Supporting Information).

Fig. 4 presents experimentally measured IFT data at 80 °C and 20 MPa, and the surfactant concentration was maintained at 0.5 wt%,

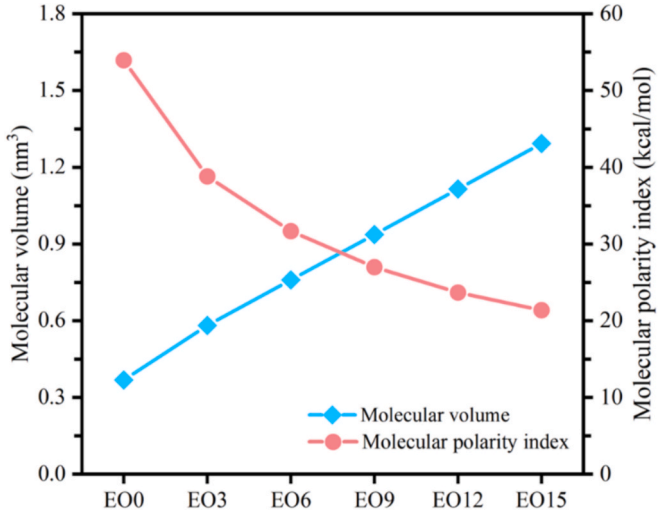

Fig. 3. Molecular volume and MPI changes of AECs with various EO chain length.

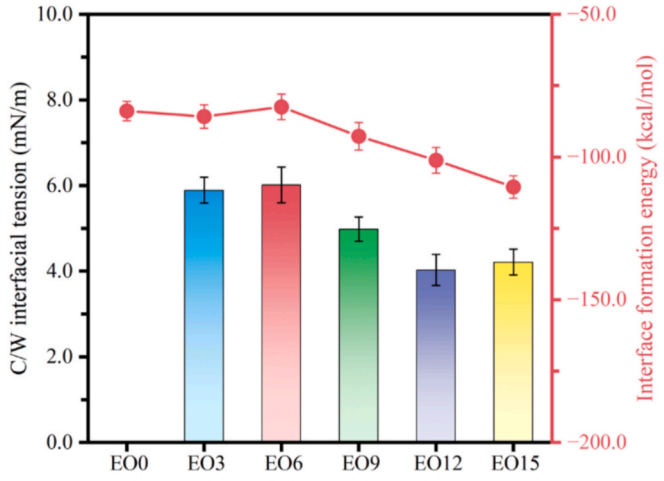

Fig. 4. The C/W interfacial tension at 80 °C and 20 MPa, along with the corresponding interface formation energy for different AEC loaded system.

which is substantially above the corresponding critical micellar concentrations (CMCs) for AEC surfactants studied. Under such high-pressure conditions, the C/W IFT exhibits only modest variation overall. EO3 and EO6 display comparable values around 6.0 mN/m. With further extension of the EO chain, the IFT progressively decreases (e.g., EO9: 5.0 mN/m) and tends to level off at approximately 4.0 mN/m for EO12 and longer chains. This trend underscores the influence of EO chain length on interfacial adsorption behavior and highlights the transition from insufficient surface activity at low EO numbers to saturated interfacial packing at higher EO levels. At HPHT, CO_2 approaches supercritical states, enhancing its compatibility with hydrophobic alkyl tails while weakening water's hydrogen-bonding capacity. Longer EO chains (≥EO9) adopt stretched conformations that bridge the C/W interface: their terminal EO segments remain hydrated (stabilizing aqueous contact), while proximal EO units interact favorably with CO_2 via dipole-induced dipole interactions. This dual affinity enables dense interfacial packing, minimizing IFT. Conversely, short EO chains (EO3) lack sufficient flexibility and steric effect; their alkyl tails partially collapse into aqueous domains under HPHT, creating interfacial voids that elevate IFT. The narrow IFT range observed under HPHT (4.0–6.0 mN/m) across all EO variants suggests a saturation effect, where EO chains beyond the critical length (EO9) no longer contribute significantly to further interfacial tension reduction due to steric limitations.

To further elucidate the thermodynamic underpinnings of the observed IFT trends, the interfacial formation energy (IFE) was calculated to quantify the adsorption stability of AEC surfactants at the C/W interface [55], which is defined as:

$$\mathrm{IFE} = \frac{E_{Total} - (nE_{AEC} + E_{Bare})}{n}$$

where E_{Total} is the total energy of the equilibrated AEC-stabilized C/W interfacial system, E_{AEC} represents the energy of a single AEC molecule, and E_{Bared} denotes the energy of the bare C/W interface without surfactants. A more negative IFE indicates stronger surfactant adsorption and a higher capacity for IFT reduction, which facilitates the formation of stable liquid lamellae in foam films. As illustrated in Fig. 4, AEC surfactants with short EO chains (EO0-EO6) display relatively constant IFE values, suggesting that the incorporation of a limited number of EO units exerts minimal influence on interfacial thermodynamics, which is also consistent with the experimental IFT results. In contrast, a marked decrease in IFE is observed when the EO number exceeds six, indicating a significant enhancement in interfacial adsorption stability. This improvement arises from the combined effects of reduced electrostatic repulsion between anionic headgroups and enhanced interfacial packing efficiency due to the conformational flexibility of longer EO chains. It is noteworthy that although IFE continues to decrease beyond EO9, the

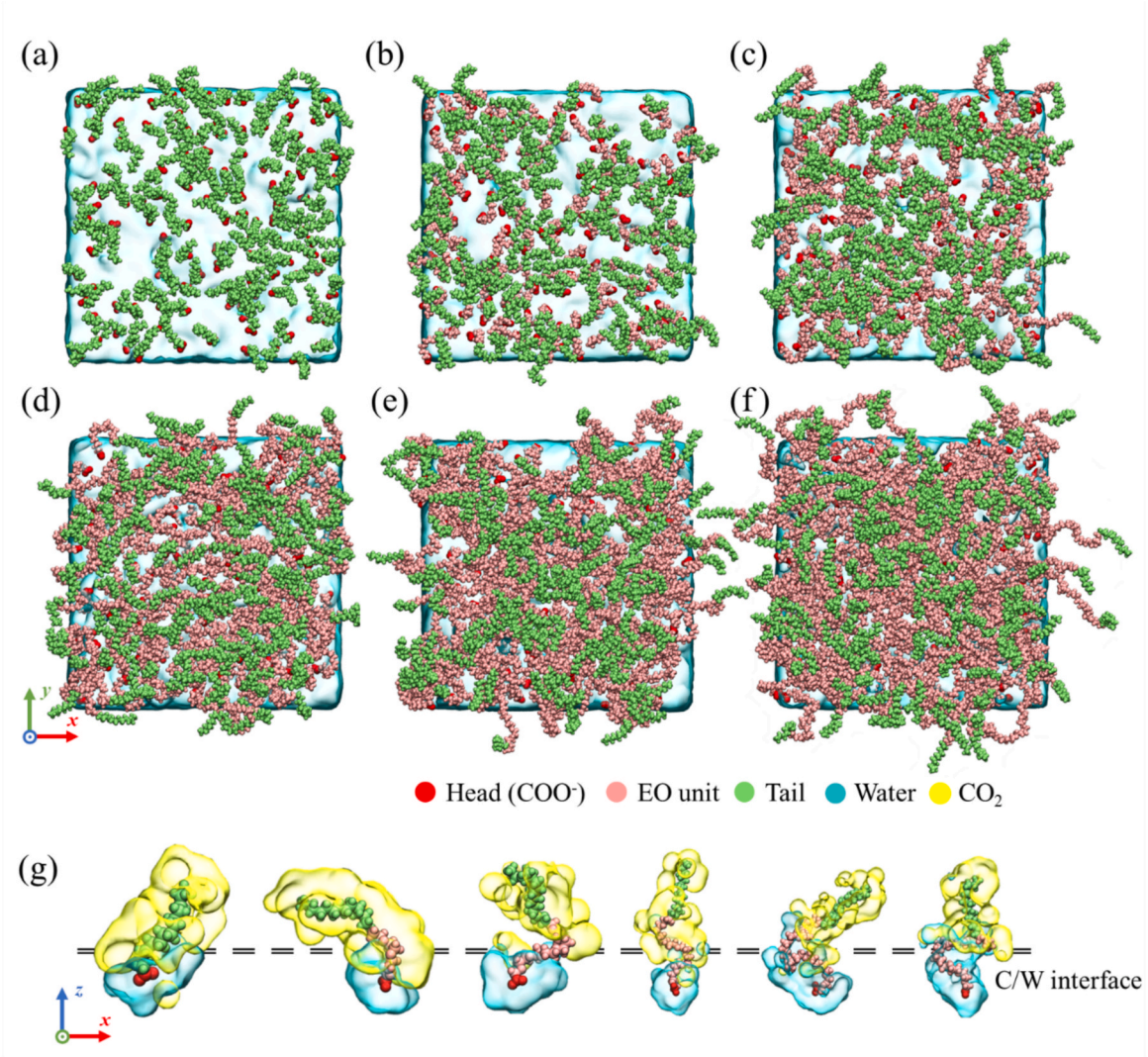

Fig. 5. Equilibrium monolayer structures at the C/W interface along the xy-plane for AECs with increasing EO chain lengths: (a) EO0, (b) EO3, (c) EO6, (d) EO9, (e) EO12, and (f) EO15, and (g) Structural representation of a single AEC monomer at the C/W interface.

experimental IFT reaches a plateau. This apparent divergence reflects the distinct nature of the two quantities: while IFE describes the molecular-level free energy gain associated with transferring an individual surfactant molecule from bulk water to the interface, IFT represents the macroscopic interfacial energy per unit area, which depends on both adsorption strength and surface saturation. Beyond a certain EO chain length, additional EO units primarily extend into the aqueous phase rather than contributing directly to interfacial packing, thus exerting minimal further reduction in IFT despite continued stabilization at the molecular adsorption level. Overall, the combined experimental and computational results underscore the existence of a critical EO chain length threshold (>6), beyond which interfacial performance is maximized due to a balance between molecular hydrophilicity, steric packing constraints, and interfacial saturation.

3.2.3. *Interfacial structuring: molecular packing and hydration*

The interfacial behavior and molecular organization of AEC surfactants at the CO_2/water interface are profoundly regulated by the number of ethylene oxide (EO) groups, as illustrated in Fig. 5. With increasing EO units, the enhanced hydration of EO chains drives a transition from sparse to densely packed interfacial monolayers. Structural partitioning analysis reveals that short EO chains (e.g., ≤6 units) exhibit partial penetration into the aqueous phase, forming discontinuous adsorption layers with nanoscale pores that facilitate direct CO_2-water contact. In contrast, longer EO chains (e.g., >6 units) undergo bending and adopt looped conformations at the interface due to steric hindrance (Fig. 5g), leading to a continuous and compact monolayer that effectively blocks molecular diffusion. These conformational changes are further supported by density profiles (Fig. 6a and Fig. S4): the hydrophilic headgroup remains fully hydrated in the aqueous phase, the hydrophobic tail extends into the CO_2 phase, while the EO segments dominate the interfacial region, acting as a dynamic structural bridge.

The hydration dynamics of EO chains, quantified through radial distribution function (RDF) analysis (see Fig. 6b–c), provide mechanistic insights into their interfacial stabilization. The oxygen atoms (O) in EO groups form strong hydrogen bonds with water molecules, with the first hydration shell of the initial EO group (e.g., O3 in AEO_9C) exhibiting a sharp RDF peak attributed to direct hydrogen bonding. As the EO number increases, the intensity of secondary hydration peaks (second and third shells) progressively rises, reflecting conformational adjustments of the EO chains and their amplified water-binding capacity. Notably, spatial heterogeneity in hydration is observed along the EO chain: front-end EO groups near the aqueous phase show stronger hydration due to unrestricted water access, while tail-end groups adjacent to the CO_2 phase display weakened interactions, emphasizing the critical role of molecular positioning in hydration efficacy.

These hydration-driven structural changes directly correlate with the evolution of interfacial layer thickness, as shown in Fig. 6d. On the aqueous side, the hydrated EO chains expand into the interfacial region, with thickness increasing monotonically as EO units grow from 0 to 15.

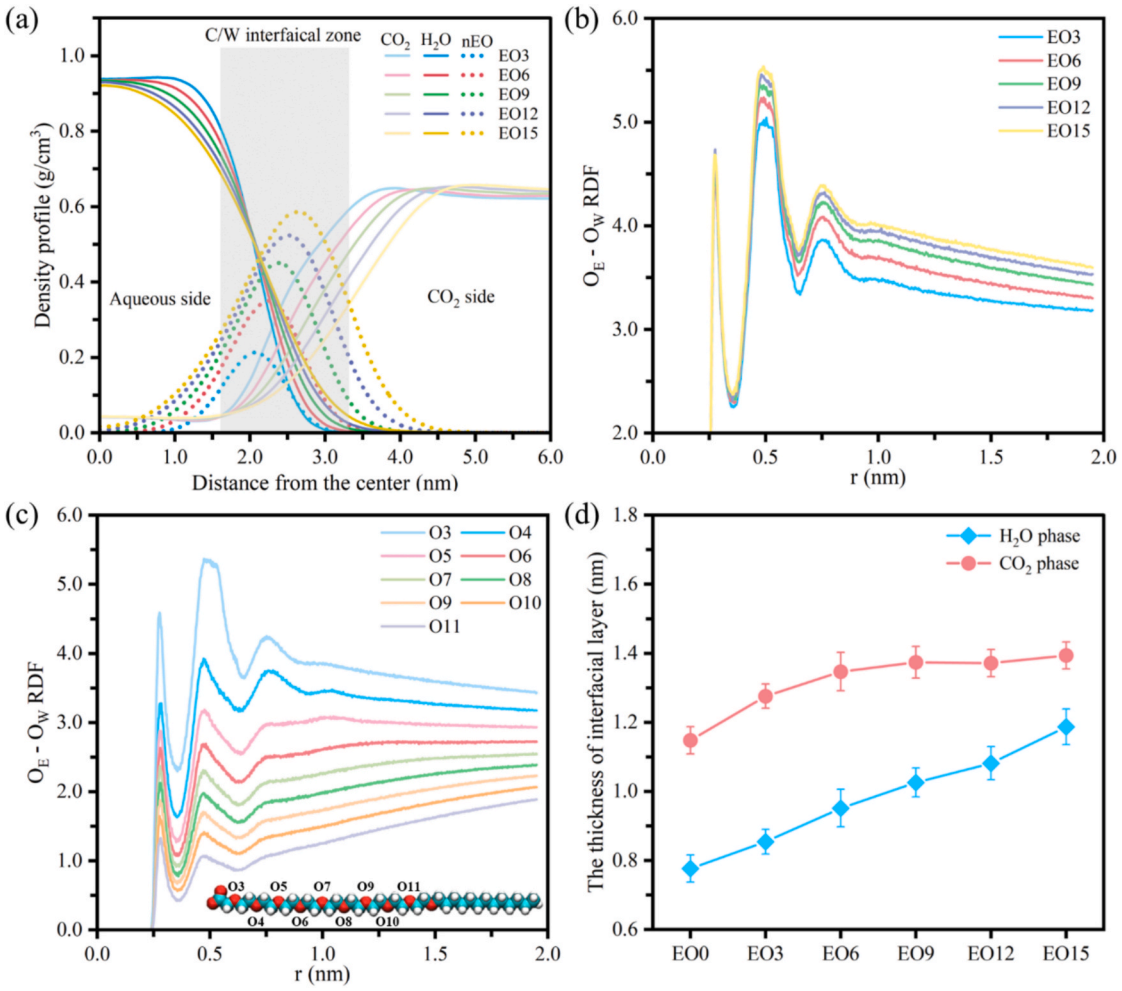

Fig. 6. (a) Interfacial density profiles of water, CO_2, and EO chains across different AEC systems, (b) RDFs between the oxygen atom (O_E) in the first EO unit and the oxygen atom (O_w) of water molecules for various AEC systems, and (c) RDF analysis of O_E and O_w interactions at the AEO_9C-loaded C/W interface, and (d) the thickness of the interfacial zones on both the aqueous phase and CO_2 phase sides, for the studied systems.

Conversely, on the CO_2 side, the thickness exhibits a saturation trend—initially rising with EO units up to 9, then plateauing beyond this threshold. Surface energy analysis reveals that at 9 EO units, the polar EO chains and nonpolar alkyl tails achieve near-equivalent interfacial coverage (~52 % vs. 48 %), marking an optimal hydrophilic-lipophilic balance (HLB). Below this threshold, hydrophobic dominance drives deeper tail penetration into the CO_2 phase, while exceeding 9 EO units forces hydrophilic EO chains to fold back toward the aqueous phase due to steric exclusion from CO_2. This HLB-governed saturation explains why additional EO units (>9) primarily stabilize the hydration layer rather than altering CO_2-side distribution.

Collectively, the EO number dictates a trade-off between interfacial permeability and blocking capability. Short EO chains prioritize aqueous compatibility and porous monolayers conducive to CO_2 diffusion, whereas long EO chains leverage steric hindrance and hydration saturation to form impermeable barriers. These findings establish a molecular design principle: tailoring EO chain length enables precise control over interfacial architecture, offering strategic advantages for applications such as CO_2-responsive foams (requiring dynamic permeability) or long-term carbon sequestration (demanding robust interfacial blocking). The interplay between hydration, conformation, and phase-specific saturation elucidated here provides a universal framework for engineering surfactants in multiphase systems.

3.3. Hydrodynamic behavior of interfacial molecules

3.3.1. Hydrogen bonding dynamics and interfacial mobility

To quantitatively assess the interfacial affinity of AEC monolayers at the C/W interface, hydrogen bonds (HBs) formed between AEC molecules and water were analyzed from the simulation trajectories. As expected, increasing the EO chain length systematically enhances HB formation, with every three additional EO groups contributing approximately 1–3 extra HBs per AEC molecule. Although longer EO chains introduce steric hindrance, the hydrogen-bonding network becomes progressively more robust. For example, AEO_9C forms up to 10–12 HBs per molecule, whereas each AEO_3C forms only 4–6 HBs. This increased hydrogen bonding correlates with the formation of more structured and rigid interfacial water layers, as the hydrophilic EO segments penetrate deeper into the aqueous phase, thereby strengthening the surfactant–water interactions.

The thermodynamic aspect of this interfacial behavior is further elucidated by the desorption energy of AEC monomer, derived from PMF analysis. As shown in Fig. 7, for alkyl carboxylates without EO chains, desorption from the C/W interface is relatively easy, with a low desorption energy of approximately 15 k_BT, indicating weak interfacial binding and facile loss of AEC surfactants. Upon the introduction of EO chains, the desorption energy gradually increases, reaching nearly 50 k_BT for the $AEO_{15}C$ surfactant (an increase of ~ 230 %). This rise reflects the additional energetic barriers associated with EO chain dehydration during desorption. The resulting metastable interfacial configuration, together with the strengthened hydrogen bonding network, contributes to the improved foam stability observed in long-chain systems, as evidenced by prolonged drainage half-lives under shear.

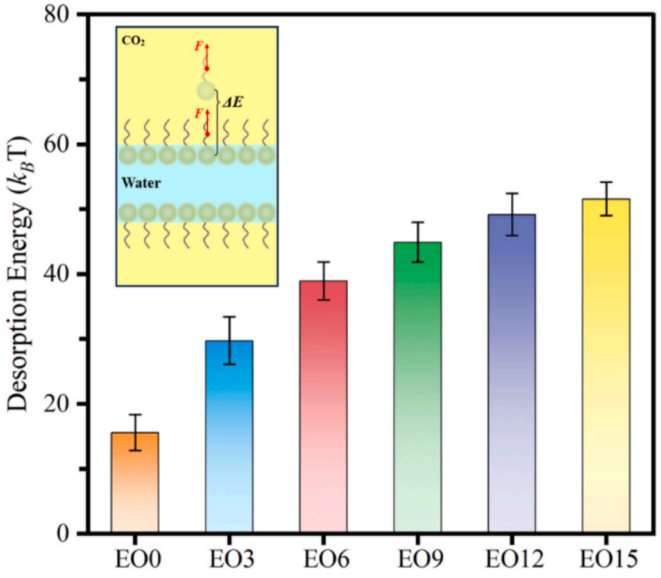

Fig. 7. The desorption energy of the AECs with varying EO chain length from the C/W interface.

However, the thermal lability of these HBs emerges as a critical limitation: elevating temperature from 50 °C to 110 °C makes the AEC-water hydrogen bonds decay much quicker, and eventually slashes HB lifetimes by nearly 50 %, as shown in Fig. 8a, destabilizing the HB network through accelerated bond breakage and reorganization. Such thermal fragility aligns with experimental observations of foam coarsening at high temperatures, where weakened interfacial viscoelasticity permits rapid gas diffusion between bubbles. Intriguingly, while heat disrupts HBs, it simultaneously activates surfactant mobility—a dual effect captured by lateral self-diffusion coefficients (Fig. 8b). At fixed EO chain length, rising temperature boosts AEC mobility at the C/W interface by nearly 100 % (e.g., AEO_9C at 50 °C diffuses 1.2×10^{-5} cm^2/s vs. 2.0×10^{-5} cm^2/s at 110 °C), as thermal energy overcomes energy barriers for interfacial hopping. This mobility surge, however, is counterbalanced by EO chain elongation, for example, AEO_9C surfactant diffuses 26 % slower than EO3 counterparts at 80 °C, their extended EO segments entangling with neighboring molecules to impose steric drag and HB-mediated friction. The resultant trade-off positions EO chains as molecular "dynamic dampers", where chain extension sacrifices repositioning agility to fortify interfacial cohesion.

In addition, the presence of salt ions further modulates this equilibrium through ion-specific interactions. Here, we compared the interfacial behavior of EO3 and EO9 systems in the presence of Na^+ and Ca^{2+} salts, with concentrations up to 10.0 wt%. As shown in Fig. 9, in sodium-dominated systems, AEC headgroup ($–COO^-$) diffusion decreases marginally (≤15 %) as Na^+ climbs from 2 % to 10 %, with EO3 and EO9 exhibiting parallel trends—a weak suppression attributed to nonspecific charge screening rather than binding. The paradigm shifts dramatically with calcium ions: 10 wt% Ca^{2+} plunges EO3 diffusion by 50 % and nearly immobilizes EO9 surfactants (4.3×10^{-6} cm^2/s), as Ca^{2+} bridges adjacent $–COO^-$ groups via multidentate coordination, effectively crosslinking surfactants into a quasi-solid matrix. Notably, EO9's superior immobilization under Ca^{2+} stems from synergy between ion-mediated crosslinking and inherent EO entanglement—a "dual locking" mechanism absent in shorter chains. This ion-specific hierarchy ($Ca^{2+} \gg Na^+$) underscores the critical role of charge density in dictating surfactant mobility, with divalent ions exerting disproportionate control over interfacial dynamics.

3.3.2. Interfacial confinements of water and CO_2 molecules

Beyond the interfacial dynamics of AEC monolayers, we also investigated the temporal evolution of water and CO_2 confinement, probed by survival probability and MSD analysis, which further reveals how EO chain length governs molecular transport across the CO_2/water interface (Fig. 10). For short-chain AECs (3–6 EO), survival probability curves decay rapidly (Fig. 10a), with 50 % of interfacial water molecules escaping within 20 ps—a hallmark of leaky interfaces where transient pores enable fast molecular exchange. In stark contrast, AEC with long EO chains (9–15 EO) exhibit prolonged interfacial retention: over 50 % of water and 40 % of CO_2 remain trapped beyond 20 ps, forming a dynamically arrested zone where surfactant-entangled EO chains and hydrogen bond (HB) networks act as molecular sieves. For interfacial CO_2 molecules, however, the EO group shows limited constraint on their mobility (Fig. 10b), and there are nearly 40 % CO_2 trapped within the

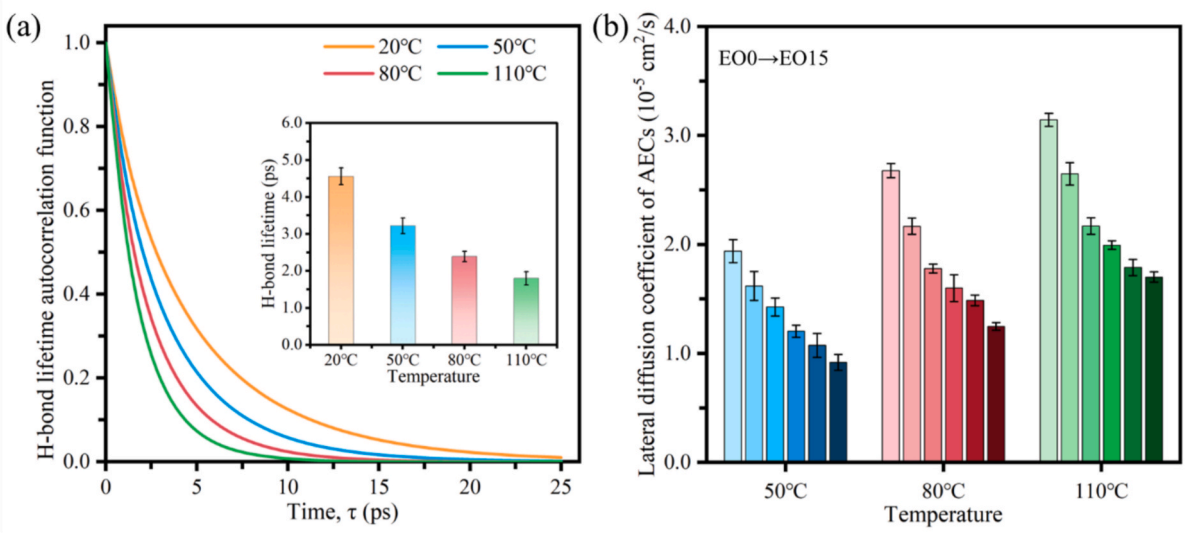

Fig. 8. (a) The autocorrelation function of H-bond lifetime between AEO_9C monolayers and interfacial water, and the insert represents the H-bond lifetime for different temperatures. (b) The lateral diffusion coefficient of AECs at the C/W interface under varying different temperature (the column from left to right represent EO0 to EO15 for each temperature).

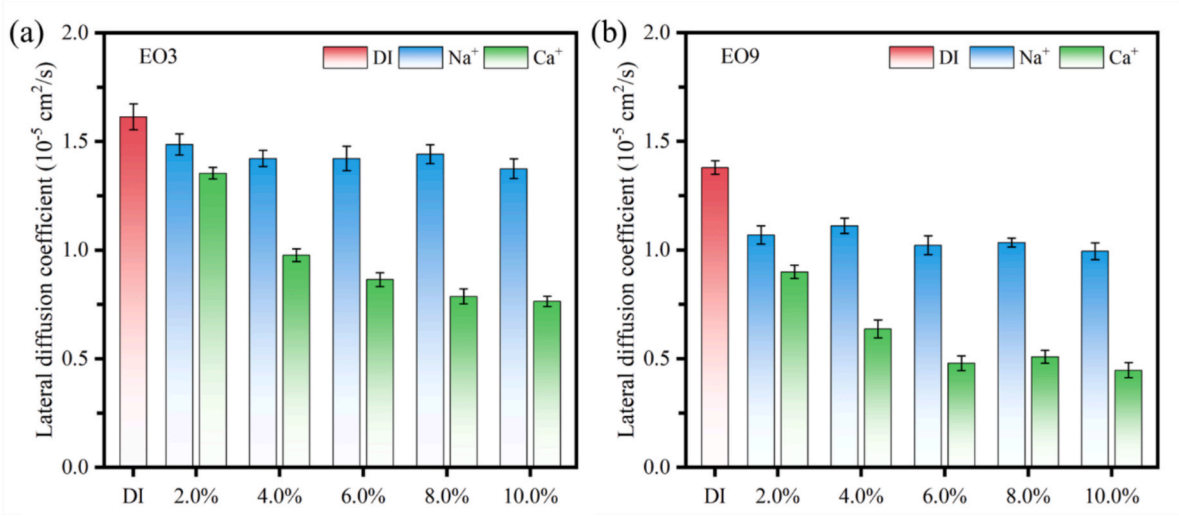

Fig. 9. The lateral diffusion coefficient of AECs at the C/W interface under varying salinity conditions.

interfacial zone as the EO chain length increase. Interestingly, when EO unit achieves 9 or over, its effect on the interfacial CO_2 molecules seems to be equilibrium, and no significant changes are observed.

The MSD of these interfacial molecules further dissect diffusion modes (Fig. 10c–d). the molecular mobility of water, both at the interface and in the bulk phase, is progressively suppressed as the ethylene oxide (EO) chain length increases in AEC surfactants, revealing a dual confinement mechanism. At the CO_2/water interface, the self-diffusion coefficient of interfacial water decreases significantly from 4.0×10^{-9} m^2/s in the EO3 system to 1.2×10^{-9} m^2/s in the EO9 system, representing a 70 % reduction. This marked slowdown arises from the combined effects of steric hindrance caused by densely packed EO chains and stabilization of the hydrogen bonding network, where extended EO segments serve as dynamic crosslinkers between interfacial water molecules. In addition, the hydrophilic nature of long EO chains allows partial penetration into the bulk aqueous phase. This behavior is not observed in conventional nonionic surfactants such as alkyl polyglucosides (APG) [25], the presence of APG monolayer at the interface exhibits no effect on the bulk water phase. These penetrating EO termini reorganize the bulk water structure through hydrogen bonding, leading to a 20–25 % reduction in bulk water diffusivity compared to EO3 systems. This distinctive ability to modulate both interfacial and bulk water mobility highlights the potential of long-chain AECs as efficient rheological modifiers in applications requiring simultaneous interfacial stabilization and bulk viscosity regulation.

In contrast to water, the mobility of interfacial CO_2 shows only moderate sensitivity to EO chain length. The self-diffusion coefficient of CO_2 decreases by approximately 10 % from EO3 to EO15. This relatively minor reduction is consistent with the lack of specific interactions between CO_2 and EO chains, as confirmed by radial distribution function (RDF) analysis, which reveals negligible accumulation of CO_2 near EO oxygen atoms. The observed decrease in CO_2 mobility is instead attributed to physical obstruction, as entangled EO chains form complex interfacial structures that force CO_2 molecules to diffuse along more convoluted pathways around the hydrophobic alkyl tails. According to survival probability analysis, this steric resistance extends the residence time of CO_2 at the interface without completely restricting its motion. This balance is particularly important for maintaining adequate CO_2

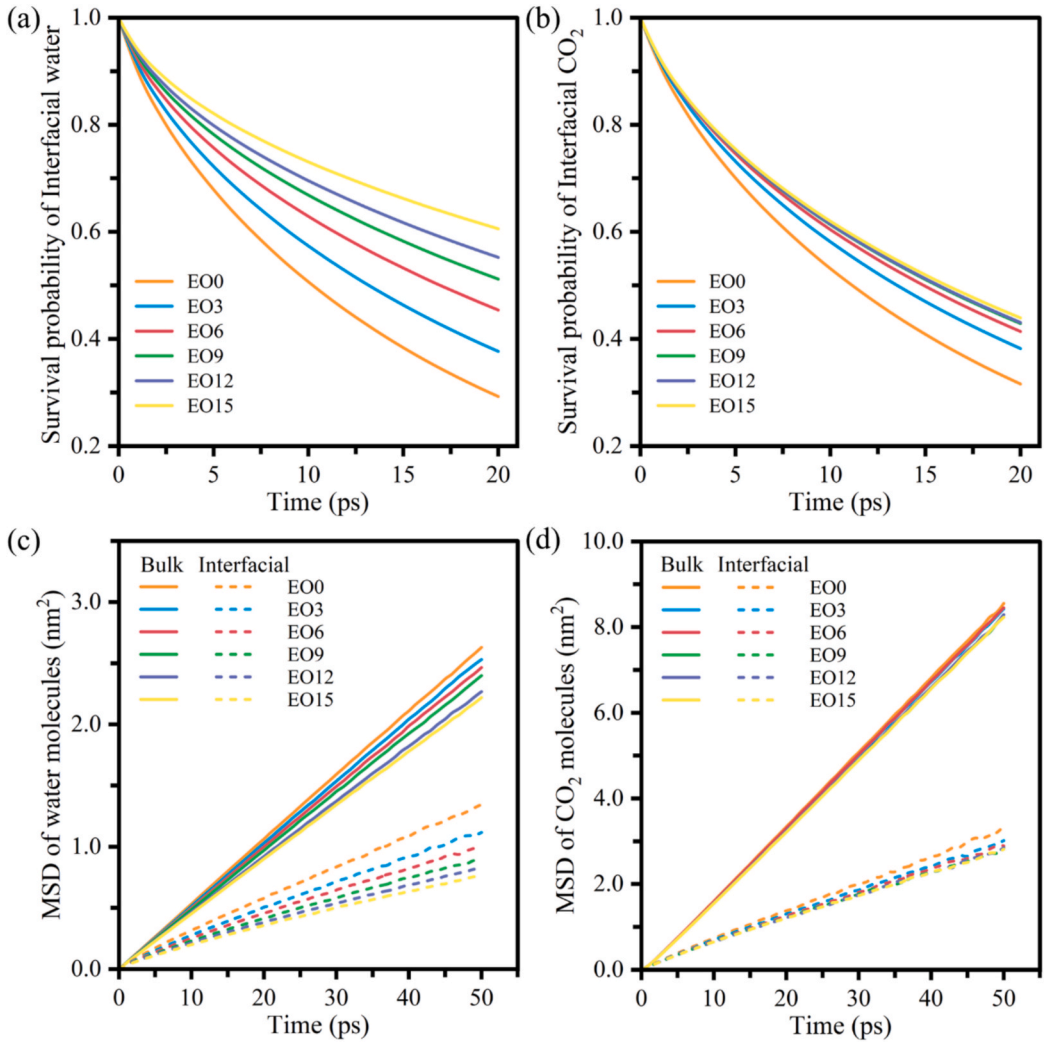

Fig. 10. Survival probability of water (a) and CO_2 (b) molecules trapped within the interfacial zone, along with the corresponding MSD curves of water (c) and CO_2 (d) molecules for different AEC-loaded systems.

exchange rates in applications such as foam-assisted enhanced oil recovery. The distinct impacts on water and CO_2 diffusion, with reductions of 70 % and 10 % respectively, underscore the selective gating effect of EO chains. These chains preferentially restrict the transport of polar species while allowing controlled diffusion of nonpolar molecules.

4. Conclusions

In this study, we systematically investigated the interfacial dynamics and structure–property relationships of AEC surfactants with varying EO chain lengths at the C/W interface, integrating experimental foam analysis with molecular simulations. Our key findings are summarized as follows:

- The foam generation and drainage behavior of AEC surfactants exhibit a non-linear dependence on EO chain length. A critical threshold around 9 EO units was identified, where interfacial adsorption kinetics and film elasticity are optimally balanced, enabling enhanced foamability and prolonged drainage half-life.
- The extension of EO chains significantly increases molecular volume and reduces polarity, thereby modulating interfacial adsorption thermodynamics and micellization behavior. Under HTHP conditions, long-chain AECs exhibit superior interfacial tension reduction, which is attributed to an optimized amphiphilic balance between hydrophilic and hydrophobic segments and enhanced interfacial packing density.
- EO chain length governs interfacial layer morphology by controlling molecular packing density and hydration structure. Long EO chains form looped conformations that construct compact, hydrated monolayers acting as molecular barriers to water and gas diffusion, while shorter chains produce porous, permeable interfaces.
- Molecular dynamics simulations reveal that EO chain elongation strengthens hydrogen bonding networks and raises desorption energy, stabilizing interfacial configurations. However, such stabilization comes at the cost of reduced lateral mobility. Temperature and salinity further modulate these dynamics, with divalent ions (e.g., Ca^{2+}) significantly immobilizing EO-rich surfactants via ionic crosslinking.
- The retention behavior of water and CO_2 molecules at the C/W interface is intricately governed by EO chain length. Long EO chains enhance interfacial confinement, reducing molecular flux and forming kinetically trapped regions with potential applications in gas barrier materials and CO_2 sequestration.

Overall, this work establishes EO chain length as a molecular design lever to fine-tune interfacial architecture, dynamics, and permeability in multiphase CO_2/water systems. These insights offer a mechanistic basis for engineering advanced C/W foaming agents and stabilizers for

subsurface energy and environmental applications.

CRediT authorship contribution statement

Jun Zhou: Writing – review & editing, Writing – original draft, Visualization, Validation, Software, Methodology, Formal analysis, Data curation, Conceptualization. **Shaopeng Li:** Writing – review & editing, Validation, Conceptualization. **Pengfei Wang:** Resources, Methodology, Conceptualization. **Ke Gao:** Writing – review & editing, Supervision, Investigation, Funding acquisition, Conceptualization.

Declaration of competing interest

The authors declare that they have no known competing financial interests or personal relationships that could have appeared to influence the work reported in this paper.

Appendix A. Supplementary data

Supplementary data to this article can be found online at https://doi.org/10.1016/j.apsusc.2025.164089.

Data availability

Data will be made available on request.

References

[1] R. Farajzadeh, A.A. Eftekhari, G. Dafnomilis, L.W. Lake, J. Bruining, On the sustainability of CO_2 storage through CO_2–Enhanced oil recovery, Appl. Energy 261 (2020) 114467, https://doi.org/10.1016/j.apenergy.2019.114467.

[2] J.R. Sminchak, S. Mawalkar, N. Gupta, Large CO_2 storage volumes result in net negative emissions for greenhouse gas life cycle analysis based on records from 22 years of CO_2 -enhanced oil recovery operations, Energy Fuels 34 (2020) 3566–3577, https://doi.org/10.1021/acs.energyfuels.9b04540.

[3] O. Massarweh, A.S. Abushaikha, A review of recent developments in CO_2 mobility control in enhanced oil recovery, Petroleum 8 (2022) 291–317, https://doi.org/10.1016/j.petlm.2021.05.002.

[4] S.M. Seyyedsar, S.A. Farzaneh, M. Sohrabi, Investigation of low-density CO_2 injection for enhanced oil recovery, Ind. Eng. Chem. Res. 56 (2017) 5443–5454, https://doi.org/10.1021/acs.iecr.7b00303.

[5] S.H. Talebian, R. Masoudi, I. Mohd, P.L.J.Z. Tan, Foam assisted CO_2-EOR: a review of concept, challenges, and future prospects, J. Petrol. Sci. Eng. 120 (2014) 202–215, https://doi.org/10.1016/j.petrol.2014.05.013.

[6] N. Kalyanaraman, C. Arnold, A. Gupta, J.S. Tsau, R.B. Ghahfarokhi, Stability improvement of CO_2 foam for enhanced oil-recovery applications using polyelectrolytes and polyelectrolyte complex nanoparticles, J. Appl. Polym. Sci. 134 (2017), https://doi.org/10.1002/app.44491 app.44491.

[7] A.U. Rognmo, S.B. Fredriksen, Z.P. Alcorn, M. Sharma, T. Føyen, Ø. Eide, A. Graue, M. Fernø, Pore-to-core EOR upscaling for CO_2 foam for CCUS, SPE J. 24 (2019) 2793–2803, https://doi.org/10.2118/190869-PA.

[8] N. Kristen-Hochrein, N. Schelero, R. von Klitzing, Effects of oppositely charged surfactants on the stability of foam films, Colloids Surf. A Physicochem. Eng. Asp. 382 (2011) 165–173, https://doi.org/10.1016/j.colsurfa.2010.12.019.

[9] A.F. Belhaj, J. Aris B M Shuhli, K.A. Elraies, S.M. Mahmood, B. Maulianda, M.S. Alnarabiji, Partitioning behaviour of novel surfactant mixture for high reservoir temperature and high salinity conditions, Energy 198 (2020) 117319. DOI: 10.1016/j.energy.2020.117319.

[10] Y. Wen, N. Lai, W. Li, Y. Zhang, Z. Du, L. Han, Z. Song, Factors influencing the stability of natural gas foam prepared by alkyl polyglycosides and its decay rules, J. Petrol. Sci. Eng. 196 (2021) 108039, https://doi.org/10.1016/j.petrol.2020.108039.

[11] J. Zhou, P.G. Ranjith, W.A.M. Wanniarachchi, Different strategies of foam stabilization in the use of foam as a fracturing fluid, Adv. Colloid Interface Sci. 276 (2020) 102104, https://doi.org/10.1016/j.cis.2020.102104.

[12] M. Firouzi, A.V. Nguyen, The Gibbs-Marangoni stress and nonDLVO forces are equally important for modeling bubble coalescence in salt solutions, Colloids Surf. A Physicochem. Eng. Asp. 515 (2017) 62–68, https://doi.org/10.1016/j.colsurfa.2016.12.004.

[13] C. Negin, S. Ali, Q. Xie, Most common surfactants employed in chemical enhanced oil recovery, Petroleum 3 (2017) 197–211, https://doi.org/10.1016/j.petlm.2016.11.007.

[14] R. Sharma, A. Desai, P. Bahadur, Hardness tolerance of anionic surfactants in the presence of nonionic surfactants, Tenside Surfactant Deterg. 40 (2003) 31–34, https://doi.org/10.1515/tsd-2003-400108.

[15] D. Levitt, S. Dufour, G.A. Pope, D.C. Morel, P.R. Gauer, Design of an ASP flood in a High-Temperature, High-Salinity, Low-Permeability Carbonate, in: 2011: p. IPTC-14915-MS. DOI: 10.2523/IPTC-14915-MS.

[16] E. Illous, J.F. Ontiveros, G. Lemahieu, R. Lebeuf, J.-M. Aubry, Amphiphilicity and salt-tolerance of ethoxylated and propoxylated anionic surfactants, Colloids Surf. A Physicochem. Eng. Asp. 601 (2020) 124786, https://doi.org/10.1016/j.colsurfa.2020.124786.

[17] J. Chen, X. Hu, Y. Fang, H. Liu, Y. Xia, Comparative Study of Conventional/Ethoxylated/Extended *n* -Alkylsulfate Surfactants, Langmuir 35 (2019) 3116–3125, https://doi.org/10.1021/acs.langmuir.8b04022.

[18] Y. Chen, A.S. Elhag, L. Cui, A.J. Worthen, P.P. Reddy, J.A. Noguera, A.M. Ou, K. Ma, M. Puerto, G.J. Hirasaki, Q.P. Nguyen, S.L. Biswal, K.P. Johnston, CO_2-in-Water foam at elevated temperature and salinity stabilized with a nonionic surfactant with a high degree of ethoxylation, Ind. Eng. Chem. Res. 54 (2015) 4252–4263, https://doi.org/10.1021/ie503674m.

[19] C. Da, S. Alzobaidi, G. Jian, L. Zhang, S.L. Biswal, G.J. Hirasaki, K.P. Johnston, Carbon dioxide/water foams stabilized with a zwitterionic surfactant at temperatures up to 150 °C in high salinity brine, J. Petrol. Sci. Eng. 166 (2018) 880–890, https://doi.org/10.1016/j.petrol.2018.03.071.

[20] J. Selvåg, T. Kuznetsova, B. Kvamme, Molecular dynamics study of surfactant-modified water–carbon dioxide systems, Mol. Simul. 44 (2018) 128–136, https://doi.org/10.1080/08927022.2017.1350783.

[21] Z. Zhang, M. Qiao, H. Zhao, Q. Ran, S. Yuan, Effect of mixed surfactants on foam stabilization: a molecular dynamics simulation, J. Mol. Liq. 365 (2022) 120096, https://doi.org/10.1016/j.molliq.2022.120096.

[22] R.M. Ziolek, F. Fraternali, A. Dhinojwala, M. Tsige, C.D. Lorenz, Structure and dynamics of nanoconfined water between surfactant monolayers, Langmuir 36 (2020) 447–455, https://doi.org/10.1021/acs.langmuir.9b03130.

[23] M. Kanduč, E. Schneck, C. Stubenrauch, Intersurfactant H-bonds between head groups of n-dodecyl-β-d-maltoside at the air-water interface, J. Colloid Interface Sci. 586 (2021) 588–595, https://doi.org/10.1016/j.jcis.2020.10.125.

[24] J. Zhou, P.G. Ranjith, Insights into interfacial behaviours of surfactant and polymer: a molecular dynamics simulation, J. Mol. Liq. 346 (2022) 117865, https://doi.org/10.1016/j.molliq.2021.117865.

[25] J. Zhou, C. Zhang, P.G. Ranjith, Highly stable polymer-enhanced pickering foams for hydraulic fracturing applications, Energy Fuels 37 (2023) 9151–9162, https://doi.org/10.1021/acs.energyfuels.3c01323.

[26] J. Li, Y. Li, Y. Song, Z. Wang, Q. Zhang, Properties of quaternary ammonium surfactant with hydroxyethyl group and anionic surfactant mixed systems, J. Mol. Liq. 271 (2018) 373–379, https://doi.org/10.1016/j.molliq.2018.08.151.

[27] J.D. Berry, M.J. Neeson, R.R. Dagastine, D.Y.C. Chan, R.F. Tabor, Measurement of surface and interfacial tension using pendant drop tensiometry, J. Colloid Interface Sci. 454 (2015) 226–237, https://doi.org/10.1016/j.jcis.2015.05.012.

[28] M.J. Frisch, G.W. Trucks, H.B. Schlegel, G.E. Scuseria, M.A. Robb, J.R. Cheeseman, G. Scalmani, V. Barone, G.A. Petersson, H. Nakatsuji, X. Li, M. Caricato, A.V. Marenich, J. Bloino, B.G. Janesko, R. Gomperts, B. Mennucci, H.P. Hratchian, J.V. Ortiz, A.F. Izmaylov, J.L. Sonnenberg, D. Williams-Young, F. Ding, F. Lipparini, F. Egidi, J. Goings, B. Peng, A. Petrone, T. Henderson, D. Ranasinghe, V.G. Zakrzewski, J. Gao, N. Rega, G. Zheng, W. Liang, M. Hada, M. Ehara, K. Toyota, R. Fukuda, J. Hasegawa, M. Ishida, T. Nakajima, Y. Honda, O. Kitao, H. Nakai, T. Vreven, K. Throssell, J.A. Montgomery Jr., J.E. Peralta, F. Ogliaro, M.J. Bearpark, J.J. Heyd, E.N. Brothers, K.N. Kudin, V.N. Staroverov, T.A. Keith, R. Kobayashi, J. Normand, K. Raghavachari, A.P. Rendell, J.C. Burant, S.S. Iyengar, J. Tomasi, M. Cossi, J.M. Millam, M. Klene, C. Adamo, R. Cammi, J.W. Ochterski, R.L. Martin, K. Morokuma, O. Farkas, J.B. Foresman, D.J. Fox, Gaussian 16 Revision A.03, (2016).

[29] A.V. Marenich, C.J. Cramer, D.G. Truhlar, Universal solvation model based on solute electron density and on a continuum model of the solvent defined by the bulk dielectric constant and atomic surface tensions, J. Phys. Chem. B 113 (2009) 6378–6396, https://doi.org/10.1021/jp810292n.

[30] T. Lu, F. Chen, Multiwfn: a multifunctional wavefunction analyzer, J. Comput. Chem. 33 (2012) 580–592, https://doi.org/10.1002/jcc.22885.

[31] J. Zhang, T. Lu, Efficient evaluation of electrostatic potential with computerized optimized code, Phys. Chem. Chem. Phys. 23 (2021) 20323–20328, https://doi.org/10.1039/D1CP02805G.

[32] T. Lu, Multiwfn Manual, version 3.8, Section 3.15.1, (2025). http://sobereva.com/multiwfn (accessed June 21, 2024).

[33] L. Martinez, R. Andrade, E.G. Birgin, J.M. Martínez, PACKMOL: a package for building initial configurations for molecular dynamics simulations, J. Comput. Chem. 30 (2009) 2157–2164, https://doi.org/10.1002/jcc.21224.

[34] K. Vanommeslaeghe, E. Hatcher, C. Acharya, S. Kundu, S. Zhong, J. Shim, E. Darian, O. Guvench, P. Lopes, I. Vorobyov, A.D. Mackerell, CHARMM general force field: a force field for drug-like molecules compatible with the CHARMM all-atom additive biological force fields, J. Comput. Chem. 31 (2009) 671–690, https://doi.org/10.1002/jcc.21367.

[35] K. Vanommeslaeghe, A.D. MacKerell, Automation of the CHARMM general force field (CGenFF) I: bond perception and atom typing, J. Chem. Inf. Model. 52 (2012) 3144–3154, https://doi.org/10.1021/ci300363c.

[36] K. Vanommeslaeghe, E.P. Raman, A.D. MacKerell, Automation of the CHARMM general force field (CGenFF) II: assignment of bonded parameters and partial atomic charges, J. Chem. Inf. Model. 52 (2012) 3155–3168, https://doi.org/10.1021/ci3003649.

[37] J.G. Harris, K.H. Yung, Carbon dioxide's liquid-vapor coexistence curve and critical properties as predicted by a simple molecular model, J. Phys. Chem. 99 (1995) 12021–12024, https://doi.org/10.1021/j100031a034.

[38] M. Bernetti, G. Bussi, Pressure control using stochastic cell rescaling, J. Chem. Phys. 153 (2020) 114107, https://doi.org/10.1063/5.0020514.

[39] G. Bussi, D. Donadio, M. Parrinello, Canonical sampling through velocity rescaling, J. Chem. Phys. 126 (2007) 014101, https://doi.org/10.1063/1.2408420.
[40] T. Darden, D. York, L. Pedersen, Particle mesh Ewald: an N·log(N) method for Ewald sums in large systems, J. Chem. Phys. 98 (1993) 10089–10092, https://doi.org/10.1063/1.464397.
[41] H. Bekker, H. Berendsen, E.J. Dijkstra, S. Achterop, R. Drunen, D. van der Spoel, A. Sijbers, H. Keegstra, B. Reitsma, M.K.R. Renardus, Gromacs: a parallel computer for molecular dynamics simulations, Physics, Computing 92 (1993) 252–256.
[42] M.J. Abraham, T. Murtola, R. Schulz, S. Páll, J.C. Smith, B. Hess, E. Lindahl, GROMACS: High performance molecular simulations through multi-level parallelism from laptops to supercomputers, SoftwareX 1–2 (2015) 19–25, https://doi.org/10.1016/j.softx.2015.06.001.
[43] W. Humphrey, A. Dalke, K. Schulten, VMD: Visual molecular dynamics, J. Mol. Graph. 14 (1996) 33–38, https://doi.org/10.1016/0263-7855(96)00018-5.
[44] M. Sega, G. Hantal, B. Fábián, P. Jedlovszky, Pytim: a python package for the interfacial analysis of molecular simulations, J. Comput. Chem. 39 (2018) 2118–2125, https://doi.org/10.1002/jcc.25384.
[45] L.B. Pártay, G. Hantal, P. Jedlovszky, Á. Vincze, G. Horvai, A new method for determining the interfacial molecules and characterizing the surface roughness in computer simulations. Application to the liquid–vapor interface of water, J. Comput. Chem. 29 (2008) 945–956, https://doi.org/10.1002/jcc.20852.
[46] J. Kästner, Umbrella sampling, WIREs Comput. Mol. Sci. 1 (2011) 932–942, https://doi.org/10.1002/wcms.66.
[47] P. Liu, E. Harder, B.J. Berne, On the calculation of diffusion coefficients in confined fluids and interfaces with an application to the liquid-vapor interface of water, J. Phys. Chem. B 108 (2004) 6595–6602, https://doi.org/10.1021/jp0375057.
[48] A. Bródka, Diffusion in restricted volume, Mol. Phys. 82 (1994) 1075–1078, https://doi.org/10.1080/00268979400100764.
[49] N. Michaud-Agrawal, E.J. Denning, T.B. Woolf, O. Beckstein, MDAnalysis: a toolkit for the analysis of molecular dynamics simulations, J. Comput. Chem. 32 (2011) 2319–2327, https://doi.org/10.1002/jcc.21787.
[50] R. Gowers, M. Linke, J. Barnoud, T. Reddy, M. Melo, S. Seyler, J. Domański, D. Dotson, S. Buchoux, I. Kenney, O. Beckstein, MDAnalysis: A Python Package for the Rapid Analysis of Molecular Dynamics Simulations, in: 2016: pp. 98–105. DOI: 10.25080/Majora-629e541a-00e.
[51] P. Smith, R.M. Ziolek, E. Gazzarrini, D.M. Owen, C.D. Lorenz, On the interaction of hyaluronic acid with synovial fluid lipid membranes, Phys. Chem. Chem. Phys. 21 (2019) 9845–9857, https://doi.org/10.1039/C9CP01532A.
[52] D.C. Rapaport, Hydrogen bonds in water: network organization and lifetimes, Mol. Phys. 50 (1983) 1151–1162, https://doi.org/10.1080/00268978300102931.
[53] Z. Liu, T. Lu, Q. Chen, Intermolecular interaction characteristics of the all-carboatomic ring, cyclo[18]carbon: focusing on molecular adsorption and stacking, Carbon 171 (2021) 514–523, https://doi.org/10.1016/j.carbon.2020.09.048.
[54] A. Al-Badi, M. Souayeh, R.S. Al-Maamari, M. Aoudia, Impact of the molecular structural variation of alkyl ether carboxylate surfactant on IFT reduction and wettability alteration capabilities in carbonates, Geoenergy Sci. Eng. 222 (2023) 211395, https://doi.org/10.1016/j.geoen.2022.211395.
[55] W. Zhang, M.-Y. Zhang, K. Wang, R. Sun, S. Zhao, Z. Zhang, Y.-P. He, F. Yu, Geometry transformation of ionic surfactants and adsorption behavior on water/ *n* -decane-interface: calculation by molecular dynamics simulation and DFT study, RSC Adv. 11 (2021) 28286–28294, https://doi.org/10.1039/D1RA04669A.